

Provided for non-commercial research and education use.
Not for reproduction, distribution or commercial use.



(This is a sample cover image for this issue. The actual cover is not yet available at this time.)

This article appeared in a journal published by Elsevier. The attached copy is furnished to the author for internal non-commercial research and education use, including for instruction at the authors institution and sharing with colleagues.

Other uses, including reproduction and distribution, or selling or licensing copies, or posting to personal, institutional or third party websites are prohibited.

In most cases authors are permitted to post their version of the article (e.g. in Word or Tex form) to their personal website or institutional repository. Authors requiring further information regarding Elsevier's archiving and manuscript policies are encouraged to visit:

<http://www.elsevier.com/copyright>



Contents lists available at SciVerse ScienceDirect

Earth and Planetary Science Letters

journal homepage: www.elsevier.com/locate/epsl

Experiments on turbulent metal-silicate mixing in a magma ocean

Renaud Deguen^{a,*}, Peter Olson^a, Philippe Cardin^b^a Department of Earth and Planetary Sciences, Johns Hopkins University, Baltimore, MD 21218, USA^b ISTERre, Université de Grenoble 1, CNRS, Grenoble, France

ARTICLE INFO

Article history:

Received 18 May 2011

Received in revised form 18 August 2011

Accepted 27 August 2011

Available online xxx

Editor: Y. Ricard

Keywords:

core formation
magma ocean
fragmentation
turbulent mixing

ABSTRACT

We compare the results of laboratory fluid dynamics experiments with theoretical models of turbulent entrainment in two-phase buoyant plumes and thermals to estimate the amount of mixing between the iron core of a planetesimal or planetary embryo and the molten silicates in a magma pool formed by its impact with a growing planet during accretion. We demonstrate experimentally that turbulent plumes in immiscible fluids fragment into droplets, and that the envelope of the droplet distribution is indistinguishable from the envelope of a turbulent plume in a single phase fluid under the same dynamical conditions, implying that turbulent entrainment concepts are applicable to immiscible fluids mixing. A series of experiments are made on the time evolution of a two-phase turbulent thermal, representing a planetesimal core, falling under its own negative buoyancy in a spherical fluid, representing an impact-produced magma pool. Two stages of mixing are observed in these experiments: the first corresponding to turbulent entrainment during free-fall of the thermal, the second corresponding to entrainment in turbulent gravity currents that form after the thermal reaches the base of the magma pool. We demonstrate that the amount of mixing between metals and silicate liquids in a magma pool depends on the Rouse number of the metal fragments and increases rapidly with the radius of the proto-planet. We derive a similarity model for metal-silicate mixing in a spherical magma pool, assuming a constant entrainment coefficient for the turbulent liquid metal phase. This model supports our experimental finding that a small metal core of an impactor will become diluted (i.e., mix) within a deep magma pool, but a large impacting core will not fully dilute before reaching the base of the magma pool.

© 2011 Elsevier B.V. All rights reserved.

1. Introduction

Evidence shows that the later stages of planetary accretion included large, energetic impacts (Kokubo and Ida, 1998). The dissipation of gravitational and kinetic energy associated with large impacts implies significant heating during accretion (Melosh, 1990); the energy released in each impact is probably sufficient to melt a substantial part of a growing planet once it reaches a radius of about ~2000 km (Pierazzo et al., 1997; Tonks and Melosh, 1993), implying that part of the separation of the core-forming metal phase from the silicate occurred in a low-viscosity magma ocean. Additional support for substantial melting early in Earth's history comes from Sm–Nd systematics, which suggest a major differentiation event of the Earth's mantle within the first ~100 My of Earth's history (Boyett et al., 2003; Boyett and Carlson, 2005; Caro et al., 2003, 2005). Differentiation of terrestrial bodies started early (Baker et al., 2005; Bottke et al., 2006; Yoshino et al., 2003), and it is now recognized that most of the mass of the Earth was accreted from already differentiated planetary bodies (Baker et al., 2005; Bottke et al., 2006; Ricard et al., 2009; Yoshino et al., 2003). How and to what extent the

metallic cores of those bodies have interacted with molten silicates are central issues for understanding core formation and its consequences on the partitioning of chemical species and heat between mantle and core.

Geochemical observations provide direct constraints on the timing and physical mechanisms of Earth core-mantle differentiation, but their full significance is somewhat obscured by our incomplete understanding of the physical mechanisms at work. Hafnium–Tungsten (Hf–W) chronometry has been used to infer a timescale for the Earth accretion, with simple models giving an accretion time less than ~30 My (Kleine et al., 2002; Yin et al., 2002). However, an important limitation of Hf–W systematics as a core formation chronometer is the degree of chemical and isotopic equilibration between metal and silicate after each impact (Halliday, 2004; Kleine et al., 2004), which is poorly constrained. The small, but resolvable, excess of radiogenic ¹⁸²W in the Bulk Silicate Earth compared to chondrites can be interpreted to indicate either rapid accretion or incomplete chemical re-equilibration between the metal phase of the impactor and the proto-Earth's mantle. Accordingly, the core formation timescale derived from W isotopic abundance is model-dependent, with an inverse trade-off between the assumed re-equilibration degree and the differentiation timescale (Halliday, 2004; Kleine et al., 2004).

Alternatively, the W isotopic ratio in the mantle can provide constraints on the degree of chemical equilibration if the timescale of

* Corresponding author.

E-mail address: rdeguen1@jhu.edu (R. Deguen).

core formation is inferred by other means. A number of recent studies used Hf–W systematics in conjunction with additional constraints on the timing of core–mantle differentiation – estimates of the timing of the Moon forming giant impact (Halliday, 2004, 2008; Kleine et al., 2004), U–Pb systematics (Halliday, 2004; Rudge et al., 2010), or accretion timescales estimated from *N*-body simulations of planetary accretion (Nimmo and Agnor, 2006; Nimmo et al., 2010) – to infer constraints on the degree of chemical equilibration between the growing planet and newly accreted material. These studies generally indicate that a relatively high fraction (30–70%) of each impactor core must have re-equilibrated with the proto-Earth's mantle to produce an Earth-like W isotopic ratio. This re-equilibration degree is rather poorly constrained, but it indicates that full re-equilibration was unlikely.

The abundance of siderophile elements in Earth's mantle provides additional evidence of chemical re-equilibration, at rather high temperature and pressure (Murthy, 1991; Wood et al., 2006). The concentration of most siderophile elements is much greater in the silicate Earth than expected from their low temperature, low pressure partitioning behavior. The mantle and core are apparently out of chemical equilibrium (Ringwood, 1966), a situation known as the 'excess siderophile problem'. The most plausible explanation for the over-abundance of moderately siderophile elements is chemical re-equilibration at high temperature and high pressure (>2000 K and 30–60 GPa), where the partitioning of a number of siderophile elements seems to be consistent with the silicate Earth composition (e.g. Chabot et al., 2005; Li and Agee, 1996). The chondritic relative abundance of highly siderophile elements probably requires an addition of 0.5% in mass of chondritic material during a "late veneer" phase (Wood et al., 2006). It is not clear how imperfect chemical equilibration would change this picture, however, or the conditions of temperature and pressure required to explain the moderately siderophile elements abundance in the silicate Earth.

The degree of chemical equilibration during iron/silicate segregation depends mostly on two factors. The first is the timescale for local chemical equilibration, compared to the timescale of metal/silicate segregation. Chemical equilibration is a relatively slow process because the transport of chemical species, even if aided by turbulent transport in the bulk of both liquid phases, is limited by diffusion in the vicinity of the metal/silicate interface. Efficient chemical re-equilibration requires a large surface/volume ratio, which requires that one of the two phases be efficiently dispersed in the other one. The second factor is the degree of physical mixing of metal and silicate, because the final composition of both phases depends on the volume of metal and silicates which have been in contact and have exchanged mass. The first condition is a prerequisite for any significant re-equilibration, but whether or not this would have any significant global effect depends on the second condition, the degree of physical mixing.

Magma oceans are favorable environments for high pressure/high temperature chemical re-equilibration. It has been conjectured that, following an impact, the core of the impactor would emulsify in silicate melt and fragment down to centimeter scale, where surface tension would inhibit further fragmentation (Ichikawa et al., 2010; Karato and Murthy, 1997; Rubie et al., 2003; Stevenson, 1990). The metal phase is envisioned to disperse in the silicate phase before raining out as sediment. The predicted scale of the iron rain drops (~1 cm) and the timescale of sedimentation allow for efficient chemical re-equilibration between metal and silicate (Rubie et al., 2003). The metal phase would then collect at the base of the magma ocean before migrating toward the core as large diapirs (Karato and Murthy, 1997; Monteux et al., 2009; Olson and Weeraratne, 2008; Samuel et al., 2010), at which point further chemical re-equilibration is unlikely to be significant (Karato and Murthy, 1997). It is not clear, however, that turbulence in a magma ocean would cascade down to centimeter scale during the falling time of the metal phase (Dahl and Stevenson, 2010).

Percolation of liquid iron in a solid or partially solid silicate matrix is another physical mechanism which can allow chemical equilibration because, although the diffusivity in solid silicate is even lower than in liquid silicate, the length scale (~silicate grain size) is small and the time scale of the flow is long. However, numerical simulations of metal–silicate segregation with a multiphase formalism (Ricard et al., 2009; Šrámek et al., 2010) suggest that the metal phase tends to quickly collect into large silicate-free metal ponds, even if initially dispersed in a solid silicate matrix, so that percolative flow naturally evolves toward diapirism, whereupon chemical interactions become insignificant.

Measurements (Liebske et al., 2005) and ab initio calculations (Karki and Stixrude, 2010) suggest that the dynamic viscosity η of peridotitic melt is low, in the range 10^{-2} – 10^{-1} Pa·s along a magma ocean isentrope. This low viscosity and the very large velocity and length scale involved during an impact imply that metal/silicate segregation in a magma ocean must have been an extremely turbulent process. In this paper, we give order of magnitude arguments and present turbulence experiments in immiscible fluid systems which support the suggestion by (Dahl and Stevenson, 2010) that the large scale metal–silicate mixing can be described by the concept of *turbulent entrainment*. We then use additional laboratory experiments to estimate the degree of physical mixing between metal and silicate in a magma ocean after a large impact.

2. Turbulent fragmentation and entrainment in immiscible fluid systems

2.1. Dimensional analysis

We expect that the fragmentation dynamics of a liquid iron mass falling in a low viscosity magma ocean depends on its velocity w , its radius r , its density ρ_m , the metal/silicate interfacial tension σ , the density contrast between metal and silicate $\Delta\rho = \rho_m - \rho_s$ where ρ_s is the density of the silicate melt, the acceleration of gravity g , and the dynamic viscosities μ_m and μ_s of the metal and silicate phases (or, alternatively, their kinematic viscosities $\nu_m = \mu_m/\rho_m$ and $\nu_s = \mu_s/\rho_s$). Since these eight variables contain three fundamental units, the Buckingham–Pi theorem dictates that liquid fragmentation processes are governed by five non-dimensional numbers, one set being:

$$Re = \frac{wr}{\nu_m}, We = \frac{\rho_m w^2 r}{\sigma}, Bo = \frac{\Delta\rho g r^2}{\sigma}, \lambda = \frac{\mu_s}{\mu_m}. \quad (1)$$

The Reynolds number Re is a measure of the relative importance of inertia and viscous forces. The Weber number We and Bond number Bo compare inertia and buoyancy forces, respectively, to interfacial tension at the metal/silicate interface.

Viscosity of liquid iron is $\sim 2 \times 10^{-3}$ Pa·s at atmospheric pressure and may be an order of magnitude larger at core pressure (de Wijs et al., 1998), while magma ocean viscosity is estimated to range from 10^{-2} Pa·s at the surface to 10^{-1} Pa·s at core–mantle boundary (CMB) pressure when it is fully liquid (Karki and Stixrude, 2010; Liebske et al., 2005). This implies $\lambda \sim 10$ in a fully liquid magma ocean. The density ratio $\Delta\rho/\rho_s$ is close to 1.

The initial velocity (just after the impact) of the iron mass is expected to be some fraction of the impact velocity, typically several $\text{km}\cdot\text{s}^{-1}$. With $\sigma \sim 1 \text{ J}\cdot\text{m}^{-2}$, $\Delta\rho = 4000 \text{ kg}\cdot\text{m}^{-3}$, $\rho_m = 7500 \text{ kg}\cdot\text{m}^{-3}$, $\nu_m = 2 \times 10^{-7} \text{ m}^2\cdot\text{s}^{-1}$ and $g = 5 \text{ m}\cdot\text{s}^{-2}$, this corresponds to $Re \gtrsim 10^{15}$ and $We \sim Bo \gtrsim 10^{14}$ for $r \gtrsim 100 \text{ km}$. The exact values do not really matter here; the important point is that all three dimensionless numbers are immense. The immense value of the Reynolds number implies that the fluids inside and outside the falling core will be extremely turbulent. That both the Weber number and the Bond number are very large implies that surface tension has a negligible effect on the large scale motions, at length scales large compared to capillarity length scales at

which interfacial forces are comparable to buoyancy forces and inertial forces.

Buoyancy forces and surface tension become comparable when the radius of curvature of the interface ℓ_{Bo} is of the order of

$$\ell_{Bo} = rBo^{-1/2} = \sqrt{\frac{\sigma}{\Delta\rho g}} \sim 1 \text{ cm}, \quad (2)$$

at which a local Bond number based on the radius of curvature would be $\mathcal{O}(1)$.

The length scale at which surface tension balances inertia can be estimated as follows in a turbulent fluid where deformation of the metal/silicate interface is due to spatial and temporal fluctuations of the velocity. Assuming a Kolmogorov turbulent cascade, then u_ℓ , the spatial fluctuations of the velocity at a length scale ℓ , varies as $u_\ell \sim (\epsilon\ell)^{1/3} \sim w (\ell/r)^{1/3}$, where $\epsilon \sim w^3/r$ is the dissipation rate, equal to the rate of kinetic energy supplied by the large scale eddies (Tennekes and Lumley, 1972). Surface tension at the scale ℓ will balance inertia if a local Weber number, $We_\ell = \rho u_\ell^2 \ell / \sigma = \mathcal{O}(1)$. This occurs at a length scale ℓ_{We} given by

$$\ell_{We} = rWe^{-3/5} = \left(\frac{\sigma}{\rho_m}\right)^{3/5} r^{2/5} w^{-6/5} \lesssim 0.5 \text{ mm}. \quad (3)$$

A similar scaling law has been proposed for the equilibrium size of droplets in a forced turbulent flow, and found to be in good agreement with experimental measurements in dilute solutions when coalescence is unimportant (Chen and Middleman, 1967; Hinze, 1955). The proportionality constant in these experiments is found to be about 0.1, from which Eq. (3) predicts an equilibrium drop size of ~ 0.05 mm for an impactor core 100 km in radius with $We \sim 10^{14}$. It is not clear however that an equilibrium drop size distribution is reached during impactor core fragmentation, so that the equilibrium size given by Eq. (3) should be seen as a lower bound of metal fragment size. Note that ℓ_{We} is relatively large compared to the Kolmogorov microscale $\ell_K = (\nu^3/\epsilon)^{1/4} = rRe^{-3/4} \sim 10^{-6} - 10^{-5}$ m, below which velocity fluctuations are viscously damped.

Because interfacial tension is not expected to play a significant role at scales $\gg 1$ cm, the global-scale dynamics of the two immiscible fluids should be similar to that of turbulent flow involving miscible fluids. The direct analog of a turbulent falling mass in miscible systems is a *turbulent thermal*—an isolated buoyant mass of fluid, in which gravitational potential energy is converted to turbulent motion, which causes mixing. Numerous laboratory experiments and theoretical studies (e.g. Batchelor, 1954; Morton et al., 1956; Turner, 1969) have shown that the evolution of such buoyant mass is governed by turbulent entrainment of ambient fluid, which results in the progressive dilution of the buoyant fluid by the ambient fluid. The effect of entrainment on the mean flow in turbulent free shear flow has been successfully accounted for by the *entrainment hypothesis* (Morton et al., 1956), in which the inward entrainment velocity u is assumed to be proportional to the magnitude of the mean flow velocity w ,

$$u = \alpha|w|. \quad (4)$$

The proportionality constant α is independent of the Reynolds number, provided that $Re \geq 10^3$, and is only a function of the type of flow considered. The validity of this entrainment assumption has been verified experimentally in turbulent free shear flow such as thermals, buoyant plumes, and jets. For turbulent thermals, laboratory experiments give $\alpha = 0.25 \pm 0.1$. The entrainment coefficient is typically smaller for plumes ($\alpha \approx 0.1$) and jets ($\alpha \approx 0.05$). Turbulent

entrainment is generally considered to be controlled by the process of *engulfment* of ambient fluid by large scale inviscid vortices. Engulfment is a large scale process, and, as proposed by (Dahl and Stevenson, 2010), surface tension should not significantly alter the efficiency of this mechanism.

2.2. Experiments

We propose that metal/silicate mixing during the fall of an impactor core can be described by an entrainment law similar to miscible fluids. Theoretical justification comes from the immense value of We and Bo , as discussed above; additional support comes from experiments shown in Fig. 1. In these experiments, a buoyant plume of oil is forced through a nozzle (diameter 5 mm or 1 cm) into a cylindrical tank filled with tap water. We use either canola oil ($\nu = 10^{-5} \text{ m}^2 \cdot \text{s}^{-1}$, $\rho = 920 \text{ kg} \cdot \text{m}^{-3}$) or a low viscosity silicon oil ($\nu = 10^{-6} \text{ m}^2 \cdot \text{s}^{-1}$, $\rho = 820 \text{ kg} \cdot \text{m}^{-3}$). Both are immiscible with water. Interfacial tension measured with a ring tensiometer is $\sigma = 18 \pm 1 \text{ mJ} \cdot \text{m}^{-2}$ for water/silicon oil, and $\sigma = 21 \pm 2 \text{ mJ} \cdot \text{m}^{-2}$ for water/canola oil at ambient temperature. By varying the exit velocity w , the nozzle radius r and the viscosity of the oil, we vary the Reynolds number (based on the nozzle diameter and exit velocity) from moderate values ($Re \sim 100$) to relatively large values ($Re \sim 10^4$), and the Weber number from $We \sim 10$ to ~ 5000 . The Bond number in these experiments is relatively small ($Bo < 10$). The viscosity ratio $\lambda = \mu_{\text{water}}/\mu_{\text{oil}}$ is about 0.1 for canola oil jets in water, and 1.2 for silicon oil jets in water. The density ratio is 0.08 for canola oil jets in water, and 0.18 for silicon oil jets in water. We use forced plumes rather than buoyant thermals because it is much easier in this configuration to reach high Weber numbers.

Shadowgraphs of the resulting steady-states plumes are shown in Fig. 1, where oil appears dark and water light. In the range of parameters explored, fragmentation is always observed, but the mechanism of fragmentation varies with We and Re . At the lowest Re and We (Fig. 1a), the plume is laminar. Break-up into oil bubbles occurs through the classical Rayleigh-Plateau capillary instability, in which the disruption of a fluid cylinder into drops results in a decrease of interfacial area (and hence of interfacial energy). When Re and We are large, the initial instabilities are shear (Kelvin-Helmoltz type) instabilities which result in small scale corrugations of the oil-water interface, as can be seen close to the nozzle in Fig. 1d and e. The transition from Rayleigh-Plateau disruption to Kelvin-Helmoltz disruption when We is increased is expected from consideration of the growth rate of each instability. The growth rate of the Rayleigh-Plateau instability scales as $\omega_{RP} \sim (\rho r^3/\sigma)^{-1/2} = We^{-1/2}w/r$, while the growth rate of the Kelvin-Helmoltz instability is an increasing function of We when surface tension is present (e.g. Chandrasekhar, 1961), so we expect Kelvin-Helmoltz instabilities to dominate over capillarity instabilities above a critical value of We . At high Re and We , the corrugations of the interface due to shear instabilities eventually evolve into drops, helped by the capillarity instabilities at small scale (Villermaux, 2007). The oil phase is effectively emulsified once these instabilities grow to large amplitude.

One important finding of these experiments is that immiscible plumes at high Re and We are geometrically similar to miscible plumes. The plume diameter increases almost linearly with distance from the nozzle, which is evidence for entrainment of the water phase in the plume. This is clear far from the nozzle, where the oil phase is emulsified (Fig. 1e), and also closer to the nozzle, where the oil plume is still mostly coherent, although the entrainment rate seems to be smaller there. Note also that the spreading rate β (plume radius as a function of distance from the nozzle) of the silicon oil plume ($\beta = 0.15 \pm 0.02$ in Fig. 1e) is comparable to what is observed in miscible plumes with comparable initial momentum and buoyancy fluxes ($\beta = 0.18 \pm 0.02$ in Fig. 1f), which suggest that the entrainment coefficient is similar when We and Re are high enough.

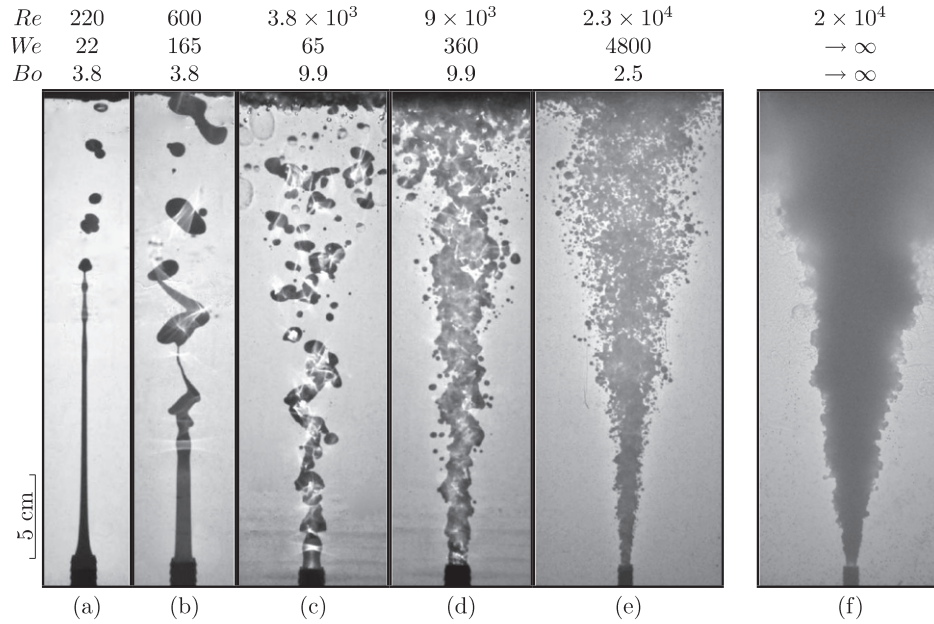


Fig. 1. Forced plumes in water. Canola oil is used in the experiments shown in a) and b) ($\lambda = 0.1$, $\Delta\rho/\rho_w = 0.08$), and a low viscosity silicone oil is used in the experiments shown in c) to e) ($\lambda = 1.2$, $\Delta\rho/\rho_w = 0.18$). f): forced plume of a water–alcohol mixture (density $\rho = 810 \text{ kg}\cdot\text{m}^{-3}$) in cold water. In a), disruption is due to the Rayleigh-Plateau capillarity instability; fragmentation is due mainly to shear instabilities in d) and e). See text for dimensional parameters values.

3. Entrainment model for metal-silicate mixing in magma oceans

Based on the experiments presented above, we hypothesize that, in spite of the iron-silicate immiscibility, the physics of turbulent entrainment are applicable to the evolution of a mass of iron falling in a silicate magma ocean. We consider a model of metal-silicate mixing as sketched in Fig. 2, in which the metallic core of an impactor is progressively mixed with molten silicate through turbulent entrainment. The silicate melt region can be either a global magma ocean of uniform depth in the case of a small body impacting a pre-existing magma ocean, or a (roughly spherical) magma pool created by the impact itself (Tonks and Melosh, 1993). First order implications of this model are discussed below.

If the entrainment assumption holds with α constant, then the radius r of the metal-silicate mixture, assumed here to remain spherical, increases linearly with depth as

$$r = r_0 + \alpha z, \quad (5)$$

(Escudier and Maxworthy (1973); Morton et al. (1956), and see Appendix A), where r_0 is the initial radius of the impactor core, and z is the vertical distance traveled by the metal-silicate mixture, with $z = 0$ being the center of mass of the iron phase just after the impact. The evolution of the metal fraction ϕ is then

$$\phi = \left(\frac{r_0}{r}\right)^3 = \left(1 + \frac{\alpha z}{r_0}\right)^{-3}. \quad (6)$$

According to Eq. (6), the core of a small body impacting a global magma ocean of depth L for which $\alpha L/r_0 \gg 1$ will be very efficiently mixed and diluted. In contrast, an impact that produces its own magma pool will have $\alpha L/r_0$ of order 1 or smaller (α is assumed to be ~ 0.25), which implies that mixing during the impactor core migration would not be complete. This later conclusion may be conservative because mixing is unlikely to cease when the iron reaches the base of the magma ocean, or even the proto-core if the mantle is completely molten. At this point, the iron mass is expected to have a significant kinetic energy, and the dissipation of this kinetic energy during subsequent flow likely involves additional mixing with the silicate phase.

The turbulent entrainment assumption leads to analytical expressions for the evolution of the volume (or equivalent radius), vertical position, and mean vertical velocity, using the equation of conservation of mass, momentum and buoyancy (Morton et al., 1956). A well-known similarity solution gives the radius of a turbulent thermal, its velocity, and its buoyancy, as functions of the distance traveled z and the total initial buoyancy B_0 as

$$r \sim z, w \sim B_0^{1/2} z^{-1}, \text{ and } g' \sim B_0 z^{-3}, \quad (7)$$

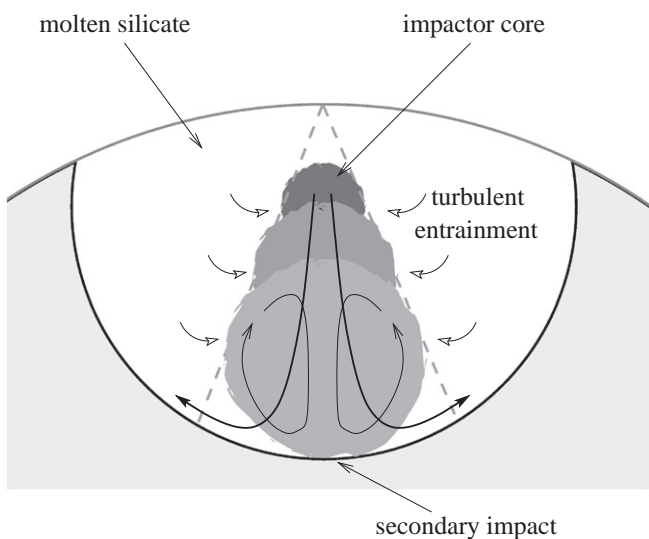


Fig. 2. A schematic view of the evolution of a large impactor core (gray) in a magma pool.

(Batchelor, 1954; Morton et al., 1956). Here $g' = g\Delta\rho\phi/\rho$ is the reduced gravity and

$$B_0 = g \frac{\Delta\rho}{\rho_s} V_0 = g'_0 V_0, \quad (8)$$

where $V_0 = (4\pi/3)r_0^3$ is the volume of iron, and g'_0 the initial reduced gravity. As can be seen from Eq. (7), the radius of a buoyant turbulent thermal grows linearly by entrainment of ambient fluid as it falls. Its initial density anomaly is progressively diluted ($g' \propto z^{-3}$) which induces a decrease of its mean vertical velocity ($w \propto z^{-1}$). The validity of Eq. (7) is supported by numerous experimental studies (see Turner (1980) for a review) and geophysical observations of atmospheric thermals and volcanic eruption clouds (Terada and Ida, 2007; Yamamoto et al., 2008). The similarity solution does not depend on initial conditions (initial velocity in particular) and is applicable at times (or distance traveled) large compared to some critical timescale (or lengthscale) where the dependence on initial conditions has vanished. We derive in Appendix A an analytical solution for the evolution of a non-Boussinesq thermal with initial momentum, slightly generalizing previous treatments (e.g. Escudier and Maxworthy, 1973; Morton et al., 1956). The similarity solution given in Eq. (7) is retrieved when the iron phase has been significantly diluted ($r \gg r_0$, or $z \gg r_0/\alpha$), and when the distance traveled is large compared to a critical lengthscale, called the Morton length, defined as

$$\ell_M = \left[\frac{(1 + \Delta\rho/\rho_s)^2 w_0^2 r_0^3}{g'_0} \right]^{1/4}, \quad (9)$$

$$\approx \left(\frac{w_0}{1 \text{ km}\cdot\text{s}^{-1}} \right)^{1/2} \left(\frac{r_0}{200 \text{ km}} \right)^{3/4} \left(\frac{g'_0}{5 \text{ m}\cdot\text{s}^{-2}} \right)^{-1/4} \times 300 \text{ km}, \quad (10)$$

above which the momentum of the metal-silicate mixture imparted by its buoyancy becomes large compared to its initial momentum. The ratio ℓ_M/r_0 is the square root of a Froude number,

$$Fr = \frac{(1 + \Delta\rho/\rho_s)w_0}{\sqrt{g'_0 r_0}}, \quad (11)$$

which characterizes the initial conditions.

Similarity conditions likely hold for a small impact, but not for the largest impacts. We derive in Appendix A an analytical expression for the mean vertical velocity of the metal-silicate mixture as a function of the distance traveled, which can be written as

$$w = \frac{\sqrt{g'_0 r_0}}{\Delta\rho/\rho_s + (1 + \alpha \frac{z}{r_0})^3} \left\{ \left(\frac{\ell_M}{r_0} \right)^4 + 2 \frac{\Delta\rho}{\rho_s} \frac{z}{r_0} + \frac{1}{2\alpha} \left[\left(1 + \alpha \frac{z}{r_0} \right)^4 - 1 \right] \right\}^{1/2}. \quad (12)$$

When $z \gg \ell_M \alpha^{-3/4}$, the initial conditions become irrelevant and Eq. (12) reduces to

$$w \approx \left(\frac{3B_0}{8\pi\alpha^3} \right)^{1/2} \frac{1}{z}, \quad (13)$$

consistent with the similarity solution Eq. (7). The vertical velocity predicted by Eq. (12) is plotted in Fig. 3 for various initial core velocities and radii. One important implication is that the velocity of the metal-silicate mixture can be very large when it reaches the bottom of the magma ocean. This *secondary impact* (metal-silicate mixture on crystalline silicate) can be energetic enough to produce additional metal-silicate mixing, although it is probably subsonic, so shock induced melting is not expected.

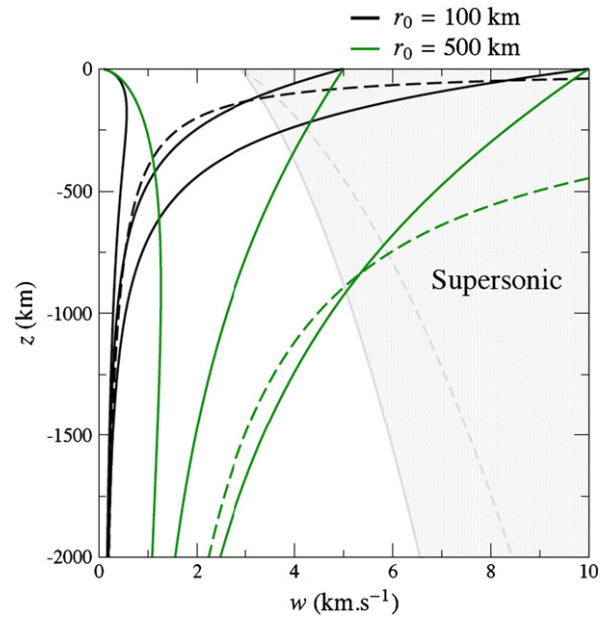


Fig. 3. Vertical velocity w of a metal-silicate volume falling in a magma ocean, as a function of distance z traveled in the magma ocean, for different values of $w_0 = w(z=0)$ and r_0 . Black and green dashed lines show the similarity solution (Eq. (13)) corresponding to $r_0 = 100$ km and 500 km. Gray solid and dashed lines are P-wave velocity in liquid MgSiO_3 (Spera et al., 2010), calculated as a function of depth for $g = 5 \text{ m}\cdot\text{s}^{-2}$ (solid line) and $g = 10 \text{ m}\cdot\text{s}^{-2}$ (dashed line). Velocities are supersonic in the gray shaded region. (For interpretation of the references to color in this figure legend, the reader is referred to the web version of this article.)

4. Evolution of the two-phase turbulent thermal

We now allow for the metal phase to be discontinuous, and model the metal phase as a concentration of discrete dense particles with a characteristic settling velocity w_s . We present experiments on two-phase turbulent thermals falling in a spherical container, with the spherical geometry of a magma pool produced by a large impact (Reese and Solomatov, 2006; Tonks and Melosh, 1993) as sketched in Fig. 2. A particular goal of these experiments is to determine the mixing following the *secondary impact* of the metal-silicate mixture at the bottom of the magma ocean. We will describe both the *free-fall phase* (the evolution before the secondary impact) and the post-impact flow.

4.1. Non-dimensional numbers

The settling velocity w_s of the dispersed phase and the diameter d_m of the container (radius r_m), or of the magma pool, provide two additional non-dimensional numbers:

$$f_0 = \frac{V_0}{V_m}, \quad \mathcal{R} = \frac{w_s}{B_0^{1/2}/d_m}. \quad (14)$$

f_0 is the ratio of the initial volume of metal V_0 to the volume of the magma pool V_m , and \mathcal{R} is the ratio of the settling velocity w_s to the typical velocity of a turbulent thermal at depth d_m as predicted by the similarity solution [$\sim B_0^{1/2}/d_m$, see Eq. (7)]. The ratio of a settling velocity to a typical flow velocity is usually referred to as a Rouse number in sedimentology, and we will follow this usage here. The Froude number is kept small (negligible initial momentum) in all experiments described below, and f_0 is usually small.

4.2. Experimental set-up and procedure

We model the iron/silicate mixture as a cloud of dense particles with settling velocity w_s . The particles are released in one of two spherical glass tanks (chemical flasks) with volume 1 L and 5 L respectively, initially filled with water (see Fig. 4). The flasks are housed in a rectangular tank filled with water in order to eliminate parallax. The release mechanism is as follows: The water/particle mixture is held in a vertically oriented plastic tube whose lower extremity is sealed using a thin latex diaphragm. Tubes of diameter 23 mm and 35 mm are used, depending on the volume released. At $t=0$, the latex diaphragm is ruptured with a needle. Movies taken during this procedure show that the diaphragm ruptures in less than 0.2 s.

We use two sizes of particles with density $2600 \text{ kg}\cdot\text{m}^{-3}$, with measured settling velocities in water of $w_s = 1.4 \times 10^{-2} \text{ m}\cdot\text{s}^{-1}$ and $8.6 \pm 1.4 \times 10^{-2} \text{ m}\cdot\text{s}^{-1}$, in agreement with the values predicted for their size and density (Dietrich, 1982). In a few small \mathcal{R} experiments, we also used aluminum flakes of density $2700 \text{ kg}\cdot\text{m}^{-3}$ with estimated settling velocity of $2 \pm 1 \times 10^{-5} \text{ m}\cdot\text{s}^{-1}$. By varying the mass of particles released, and using the different containers and particle sets, we have been able to explore a relatively large range of Rouse number \mathcal{R} . In addition to particle experiments with finite \mathcal{R} , the limit $\mathcal{R} \rightarrow 0$ can be approximated in the same device with chemically buoyant salt water thermals.

The experimental apparatus is illuminated from the side by a light sheet and the flow is recorded by a color video camera at 24 frames per second. In most experiments, the particles are released with a small amount of water dyed with fluorescein, which allows direct visualization of mixing between the dyed released fluid and the ambient. Because fluorescein has a narrow emission band, it is possible to filter a posteriori the video frames to eliminate the contribution of the dyed fluid, thus isolating the particle laden fluid (see Fig. 5b). In each video frame, we estimate the area of particle laden fluid and dyed fluid with a pixel intensity threshold method. The volume of particle laden fluid and dyed fluid is estimated with the assumption of axisymmetry of the flow. This is only approximate, because departures from axisymmetry arise from imperfect release of the payload, and from the fact that the flow is turbulent and inherently three dimensional in most experiments. Errors are estimated by repeating experiments several times. Additional uncertainties come from the somewhat arbitrary choice of the pixel intensity threshold. When estimating the volume of particle laden fluid, the resulting uncertainty is small when the fluid is concentrated in particles, but the sensitivity of the volume estimate on the threshold value becomes important when the concentration of particles becomes small, with uncertainties possibly as large as 20%. Entrainment is estimated from the measured area A of the dyed particles–water mixture and the position of its center in each video frame. The equivalent radius r_{eq} of the mixture is then calculated from the area ($r_{eq} = \sqrt{A/\pi}$) and the entrainment

coefficient is estimated by regression from the values of r_{eq} as a function of position of the center of mass of the mixture.

4.3. Free-fall phase

The results of our experiments in the free-fall phase are in qualitative and quantitative agreement with previous experiments on the sedimentation of a particle cloud (Bush et al., 2003; Noh and Fernando, 1993). Following release, the particles initially behave collectively, falling at a velocity significantly larger than their individual settling velocity. The dense particles act as volumetrically distributed buoyancy and the particle cloud evolves like a turbulent thermal, entraining ambient fluid as it falls. The evolution of the particle cloud volume and velocity are well described by the standard theory of turbulent thermals, with an entrainment coefficient $\alpha \approx 0.25 \pm 0.1$, in agreement with experiments on chemically and thermally driven turbulent thermals. Because of momentum dilution through entrainment, the particle cloud decelerates and eventually reaches a condition in which the turbulence intensity within the cloud is too weak to carry individual particles. At this point, the particles separate from the entrained fluid and fall at their settling velocity, with no further entrainment of ambient fluid (Fig. 5a). As can be seen in Fig. 6a, the particle cloud continues to spread slightly with falling distance, which may indicate particle–particle interactions.

The critical distance at which the particles separate from the entrained fluid can be estimated if the particle cloud is assumed to have reached the self-similar regime before particle fallout. Assuming a cloud velocity $w \sim B_0^{1/2}/z$ as in Eq. (13), the critical distance z_c at which the cloud velocity falls below the particles settling velocity is

$$z_c \sim \frac{B_0^{1/2}}{w_s} \quad (15)$$

(Buehler and Papantoniou, 2001; Bush et al., 2003). This prediction is found to be in good agreement with previous experimental results (Bush et al., 2003). In our experiments, particle separation depends on whether the fallout distance as predicted by Eq. (15) is greater or smaller than the diameter of the container. Since the Rouse number $\mathcal{R} \sim d_m/z_c$, the particles are expected to behave collectively and be in the thermal regime when they impact the bottom of the flask if \mathcal{R} is small, while separation of the particles from the entrained fluid is expected when \mathcal{R} is large. This is what our experiments show, as can be seen in Fig. 5. The critical value of \mathcal{R} is about 1.

4.4. Post-impact flow

The evolution of the particle cloud after impact at the bottom of the container depends on whether the particle cloud is in the turbulent thermal regime. When $\mathcal{R} \geq 1$, the particles sediment when they reach the bottom of the container (Fig. 5a) and no additional mixing is observed. When $\mathcal{R} \leq 1$ however, the inertia of the particle–water thermal drives an upward flow along the walls of the container which promotes further entrainment of ambient fluid in the particle–water mixture (Fig. 5b and c).

From snapshots taken during the experiments, we estimate the volume fraction f occupied by the particle laden fluid (i.e. the ratio of the volume of particle laden fluid to the volume of the container) as a function of time. The evolution of f for experiments with $\mathcal{R} = 0.37$ and $\mathcal{R} = 10.2$ is shown in Fig. 7, together with the height h of the particle cloud barycenter, in which time is normalized by $\tau = d_m^2/B_0^{1/2} = d_m/w(d_m)$. Three different stages denoted 1 to 3 can be identified in the evolution of the flow in Fig. 7. Stage 1 corresponds to free fall, with an increase of f due to turbulent entrainment and growth of the particle cloud. Stage 1 ends when the particle cloud reaches the bottom of the container, at $t/\tau \approx 0.25$. In the $\mathcal{R} = 10.2$ experiment, the particles sediment at this time. In contrast, in the $\mathcal{R} = 0.37$ experiment, the inertia of the

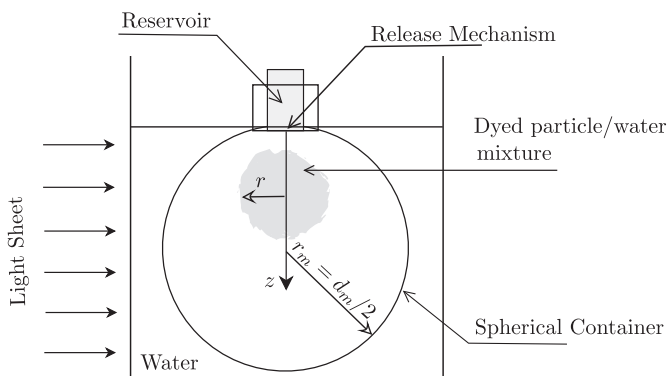


Fig. 4. Experimental set-up for turbulent thermals experiments.

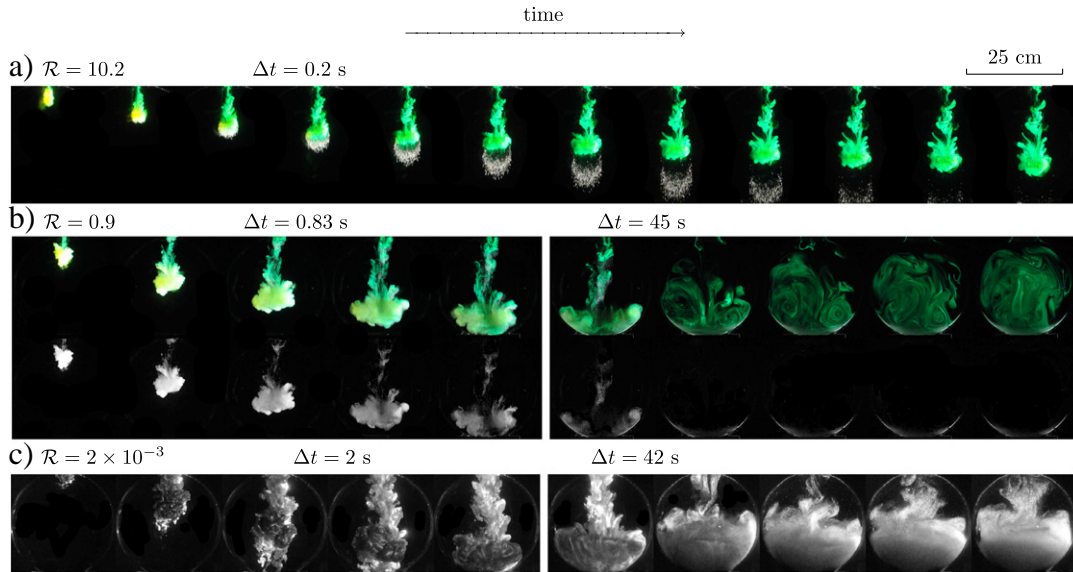


Fig. 5. Successive snapshots during the fall of a particle cloud with $\mathcal{R} = 10.2$ (payload mass $m = 0.5$ g, $w_s = 8.6 \times 10^{-2} \text{ m} \cdot \text{s}^{-1}$, $d_m = 0.207$ m), 0.9 ($m = 1.7$ g, $w_s = 1.4 \times 10^{-2} \text{ m} \cdot \text{s}^{-1}$, $d_m = 0.207$ m), and 2×10^{-3} ($m = 1$ g, $w_s = 2 \times 10^{-5} \text{ m} \cdot \text{s}^{-1}$, $d_m = 0.207$ m). a) and b)—The payload consists of a known mass of dense particles (white) and a small volume of water dyed with fluorescein (green). In the $\mathcal{R} = 0.9$ case, unfiltered snapshots are shown in the upper row, while in the lower row, the Red band of the (RGB) snapshots are shown. This allows visualization of the particles only. c)—Cloud consisting of aluminum flakes in water. In each subfigure, Δt is the time lag between two successive snapshots. The scale is the same in all pictures. (For interpretation of the references to color in this figure legend, the reader is referred to the web version of this article.)

particle cloud drives a flow which is forced by the spherical container to have a large upward component [stage 2], as can be seen in the increase in h apparent in Fig. 7. There is a further increase in f due to additional mixing during this phase, with f reaching a maximum value $f_{max} = 0.55$ in this experiment, which means that more than half of the ambient fluid has been entrained and mixed with the particle laden fluid. Turbulence decay due to viscous dissipation then allows for the progressive sedimentation of the particles [stage 3]. After reaching a maximum, f decreases due to the progressive sedimentation of the particles. Note that, after sedimentation of the particles, the residual inertia of the entrained fluid is usually large enough to allow complete mixing in the container, as can be seen in Fig. 5b.

The maximum value of f_{max} is a quantity of interest for core-mantle chemical partitioning since, for a given impactor size, it gives the volume of silicate melt which has been mixed with the metal phase during post-impact metal-silicate segregation. In our experiments, f_{max} is a

function of the three non-dimensional parameters, \mathcal{R} , Re and f_0 . It can be expected to be independent of Re if $Re \gg 1$ (Reynolds similarity). It is also expected to be independent of f_0 if $f_0 \ll 1$ ($r_0 \ll d_m$) since, if $\mathcal{R} \ll 1$, the particle cloud is expected to reach the turbulent thermal self-similar regime, which does not depend on the initial conditions. No significant dependence on f_0 has been observed in our experiments, which supports the assumption that f_{max} is primarily a function of \mathcal{R} . Fig. 8 shows the value of f_{max} as measured in our experiments as a function of \mathcal{R} . Little mixing is evident when $\mathcal{R} > 1$. For $\mathcal{R} < 1$ there is a sharp increase in f_{max} as \mathcal{R} decreases. Experiments using aluminum flakes with small \mathcal{R} , as well as experiments with chemically buoyant thermals instead of particles ($\mathcal{R} \rightarrow 0$), show a plateau with $f_{max} \approx 0.7 - 0.8$ at small \mathcal{R} . Based on our experiments, we predict significant large scale metal-silicate mixing in a magma pool when \mathcal{R} is small.

5. Applications

The experiments described in the previous section indicate that the regime of metal sedimentation and the amount of metal/silicate mixing depend critically on the value of the Rouse number. We now

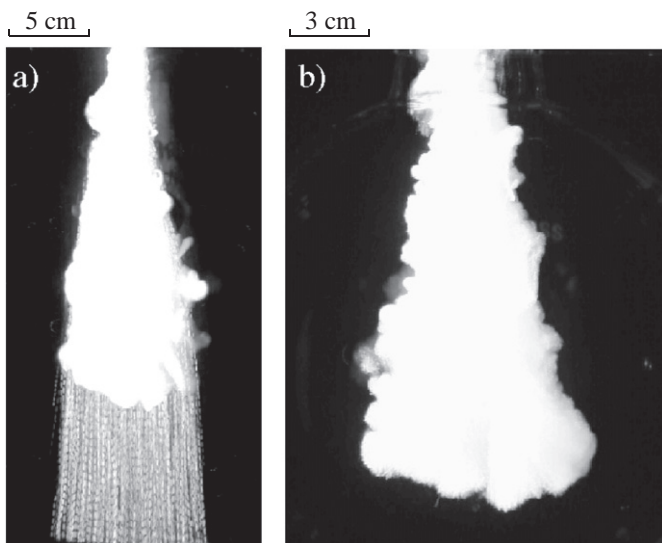


Fig. 6. Evolution of particle clouds during the free fall phase. Long exposure pictures of the fall of a particle cloud with $\mathcal{R} = 10.2$ (a) and $\mathcal{R} = 0.9$ (b) respectively.

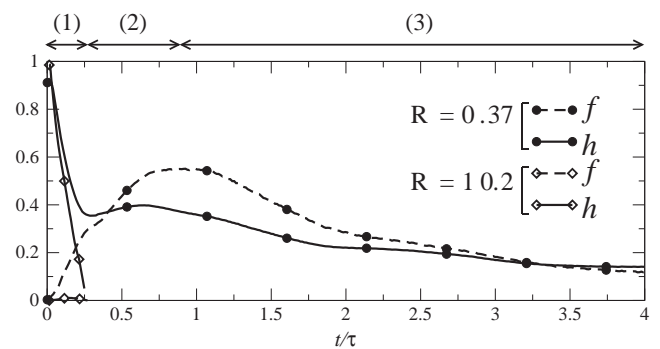


Fig. 7. Volume fraction f occupied by the particle cloud, and non-dimensional height h of the barycenter of the particle cloud versus non-dimensional time ($h = 0$ and 1 at the bottom and top of the container, respectively), during experiments with $\mathcal{R} = 0.37$ (black circles) and $\mathcal{R} = 10.2$ (open diamonds). (1) Free fall phase. (2) Upward inertia driven flow. (3) Sedimentation.

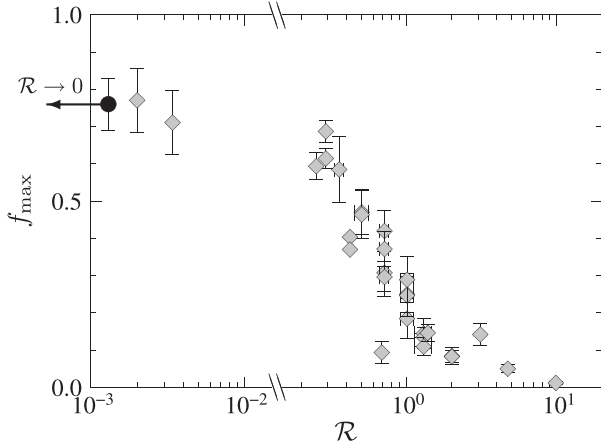


Fig. 8. Maximum value of the particle volume fraction f for a different \mathcal{R} values in particle cloud experiments. Gray diamonds denote particle cloud experiments. The black circle and error bars denote the average value and standard deviation of f_{\max} in a series of experiments with chemically buoyant salt water thermals, for which $\mathcal{R} \rightarrow 0$. The mixing efficiency increases rapidly with decreasing \mathcal{R} when $\mathcal{R} < 1$, while very little mixing occurs for $\mathcal{R} > 1$.

discuss under which conditions iron/silicate segregation would proceed in the large and small \mathcal{R} regimes.

The settling velocity of iron drops/blobs of radius a can be written as

$$w_s = \left(\frac{8 \Delta \rho}{3 C_d \rho_s} g a \right)^{1/2}, \quad (16)$$

where C_d is the drag coefficient. C_d is poorly constrained for liquid drops, but is expected to reach a constant value at high Re (Newton regime), probably smaller than 0.1 when the viscosity ratio is larger than 1 (Clift et al., 1978). The Rouse number is then given by

$$\mathcal{R} = \frac{d_m w_s}{B_0^{1/2}} \approx \left(\frac{8 r_m^2 a}{\pi C_d r_0^3} \right)^{1/2}, \quad (17)$$

which implies that $\mathcal{R} \ll 1$ if $a \ll \pi C_d r_0^3 / 8 r_m^2$. The value of \mathcal{R} and the mode of sedimentation therefore depend both on the efficiency of fragmentation and on the relative sizes of the impactor core and the protoplanet melt region.

Semi-analytical models and numerical simulations of large impacts (Bjorkman and Holsapple, 1987; Pierazzo et al., 1997; Pierazzo and Melosh, 2000; Tonks and Melosh, 1993) predict that the ratio of the melt volume to the impactor volume varies as $\gamma U^2/E_M$ with the proportionality constant $\gamma \approx 0.15$, where U is the impact velocity and E_M is the specific energy of the Hugoniot state which isentropically intersects the liquidus at 1 bar. A typical value for dunite is $E_M = 9 \times 10^6 \text{ J} \cdot \text{kg}^{-1}$ (Pierazzo et al., 1997). This scaling is applicable to vertical impact with $U^2/E_M \leq 50$ (Pierazzo et al., 1997, Fig. 11). The volume of melt is a small fraction of the impactor volume V_{imp} for $U^2/E_M \leq 20$ (Pierazzo et al., 1997). The results of Pierazzo and Melosh (2000) suggest that this scaling overestimates the melt production by $\sim 20\%$ for an impact with a 45° impact angle, and up to a factor 2 for an impact with 30° impact angle. U should be close to the escape velocity $\sqrt{2gR_p} = \sqrt{8\pi G \rho / 3 R_p}$ during oligarchic growth (Kokubo and Ida, 1998), so the melt volume should scale as

$$\frac{V_m}{V_{\text{imp}}} \approx \gamma \frac{8\pi G \rho R_p^2}{3 E_m}, \quad (18)$$

where R_p is the proto-planet radius, ρ its mean density, and G is the gravitational constant.

Using the scaling (Eq. (18)) to estimate r_m as a function of r_0 (assumed to be half the impactor radius), we find that $\mathcal{R} \ll 1$ if a is small compared to a critical value a_c given by

$$a_c = \frac{\pi^{1/3} 3^{2/3}}{128} C_d \left(\gamma \frac{G \rho R_p^2}{E_m} \right)^{-2/3} r_0 \quad (19)$$

$$\approx 0.01 \left(\frac{E_m}{9 \times 10^6 \text{ J} \cdot \text{kg}^{-1}} \right)^{2/3} \left(\frac{R_p}{3000 \text{ km}} \right)^{-4/3} r_0. \quad (20)$$

This implies that \mathcal{R} would be small if the typical fragment size is less than 1% of the impactor core radius. A consequence is that significant mixing is expected when fragmentation is efficient enough to allow chemical re-equilibration (cm to meter-sized iron fragments). Far less mixing is expected if the typical fragment size is similar or larger than a_c . In the more general case where the iron fragments are distributed over a size spectrum, it might be expected that the larger fragments remain at the base of the magma ocean when they first reach it, whereas fragments smaller than the critical size remain in suspension and become mixed with the molten silicate.

An estimate for the mixing following an impact can be obtained using the results of our experiments and the melt production after an impact predicted by Eq. (18). The quantity of interest is the dilution \mathcal{D} of the metal phase into the silicate phase, defined as the ratio of the metal volume to the silicate volume involved in the mixing. This quantity is of primary importance for chemical fractionation between core and mantle because, along with the partitioning coefficients, it determines the actual mass transfer between metal and silicate. The volume of silicate melt which has been mixed with the metal phase is $f_{\max} V_m$. If the volume of metal in suspension is assumed to be nearly equal to the impactor core volume, then the dilution is $\mathcal{D} = f_{\max} V_m / V_{\text{imp}}$. According to Eq. (18), $V_m / V_{\text{imp}} \propto R_p^2$, a consequence of the increase with planetary mass of gravitational energy released per impactor mass (Pierazzo et al., 1997), which implies a tendency for increasing dilution and efficiency of chemical transfer between metal-silicate as the accretion proceeds.

6. Implications

Our experiments on two-phase plumes in oil and water support the interpretation that the liquid metal phase of planetesimals and planetary embryos undergoes substantial turbulent fragmentation following impact in a magma ocean. Our experiments also demonstrate that the concept of turbulent entrainment is applicable to mixing processes in immiscible fluid plumes, which allows us to model the amount of turbulent metal-silicate mixing during segregation of the metal in a magma ocean using classical entrainment concepts.

We find that small iron cores falling in a deep magma ocean are expected to be efficiently diluted by entrainment. In contrast, large impactor cores would only partially mix with the silicate phase before reaching the bottom of the magma ocean. The critical parameter is $\alpha L / r_0$, where α is the entrainment coefficient, L the depth of the magma ocean, and r_0 the initial radius of the iron core. Large values of this parameter imply efficient dilution. Our experiments show that the secondary impact of partially-diluted metal at the bottom of the magma ocean generates a second episode of turbulent entrainment, which results in significant additional mixing. The total dilution of the metal phase in the molten silicate due to entrainment during the free fall and the secondary impact stages depends on the amount of melting produced by the impact, and is therefore expected to increase with increasing planetary radius.

As discussed in the introduction, the chemical partitioning between metal and silicate depends on the mass of metal and silicate which have equilibrated, i.e. the dilution of the metallic phase in the molten silicate phase. Moderately siderophile elements that become

less siderophile at high P (e.g. Ni and Co) would find themselves in excess in the metal phase, and re-equilibration must involve a transfer of these elements from metal to silicate. The net mass transfer required to ensure thermodynamic equilibrium depends on the dilution of the metal phase in the silicate phase: Increasing dilution results in more efficient extraction of moderately siderophile elements from the metal phase, which results in the silicate phase being more enriched in these elements, and the metal phase being more depleted.

Our analysis is based on the larger-scale fluid dynamical considerations; the role of smaller-scale processes needs further investigation. For example, although the equilibrium drop size in a turbulent metal-silicate mixture predicted by Eq. (3) is small enough to allow efficient chemical equilibration (Rubie et al., 2003), it is not clear that such a small size will be reached during iron segregation. The evolution of size distribution can be addressed in the context of experiments similar to the experiments presented here.

Acknowledgments

We would like to thank H.J. Melosh and an anonymous reviewer for their constructive comments, Mike Bergman for his help carrying out some of the experiments presented in Section 2, and Maylis Landeau for comments on the manuscript and discussions.

RD and PO gratefully acknowledge support from the Geophysics Program of the National Science Foundation through grant EAR-0909622.

Appendix A. Evolution of a non-Boussinesq turbulent thermal with initial momentum

We present here a model of the evolution of a turbulent, non-Boussinesq thermal with initial momentum. The model is a simple extension of already published models. By 'non-Boussinesq', we mean here that the density difference between the turbulent thermal and the ambient fluid may not be small compared to the ambient fluid density, and must be taken into account in the inertia term. We do not include dissipative heating and adiabatic heating however, the thermally induced buoyancy being assumed small compared to the chemically induced buoyancy (metal phase fraction).

We consider a buoyant spherical mass of initial radius r_0 and density $\rho_a + \Delta\rho$ released at $t=0$ with an initial (downward) velocity w_0 in a fluid of density ρ_a . The buoyant mass has an initial momentum

$$M_0 = (\rho_a + \Delta\rho)V_0w_0 \quad (\text{A.1})$$

where $V_0 = (4\pi/3)r_0^3$ is the initial volume. The buoyancy of the turbulent mass,

$$B = g \frac{\rho - \rho_a}{\rho_a} V = g'V, \quad (\text{A.2})$$

has an initial value

$$B_0 = g \frac{\Delta\rho}{\rho_a} V_0 = g'_0V_0. \quad (\text{A.3})$$

Here $V = \frac{4}{3}\pi r^3$ is the volume of the turbulent fluid in terms of its mean radius r , $g' = g(\rho - \rho_a)/\rho_a$ is the reduced gravitational acceleration, ρ is the turbulent fluid density, and the subscript '0' denotes initial values.

We adopt the usual entrainment assumption of Morton et al. (1956) and assume that the local inward entrainment velocity u is

proportional to the magnitude of the mean vertical velocity w of the thermal,

$$u = \alpha|w|. \quad (\text{A.4})$$

Experiments on non-buoyant 'puffs' (turbulent isolated masses of fluid with initial momentum) suggest that the magnitude of the entrainment coefficient is very similar to that measured for turbulent thermals (Diez et al., 2003; Richards, 1965), and we therefore assume that α remains constant, whether the evolution of the turbulent mass is governed by its initial momentum or its buoyancy. With this assumption, the equation of conservation of mass is

$$\frac{d(\rho r^3)}{dt} = 3r^2\rho_a\alpha|w|, \quad (\text{A.5})$$

while conservation of momentum and buoyancy, in absence of density stratification in the ambient fluid, give

$$\frac{4\pi}{3} \frac{d(\rho r^3 w)}{dt} = \rho_a B, \quad (\text{A.6})$$

and

$$\frac{dB}{dt} = 0, \quad (\text{A.7})$$

(Morton et al., 1956). Conservation of buoyancy requires that $B = B_0$ at each time. Some models include in the momentum equation a drag term, and also introduce a coefficient of added mass, which accounts for the momentum imparted to the surrounding fluid (Escudier and Maxworthy, 1973). The importance of these two terms appears to be negligible in laboratory experiments (Bush et al., 2003), and we will ignore them here.

We now non-dimensionalize length by r_0 , time by $(r_0/g'_0)^{1/2}$, velocity by $(r_0g'_0)^{1/2}$, and express density in terms of the metal volume fraction ϕ as $\rho = \rho_a + \Delta\rho\phi$. In non-dimensional form, the conservation Eqs. (A.5)–(A.7) then become

$$\frac{d}{d\tilde{t}} \left[(1 + \Delta\phi)\tilde{r}^3 \right] = 3\alpha\tilde{r}^2|\tilde{w}|, \quad (\text{A.8})$$

$$\frac{d}{d\tilde{t}} \left[(1 + \Delta\phi)\tilde{r}^3\tilde{w} \right] = 1, \quad (\text{A.9})$$

$$\phi\tilde{r}^3 = 1, \quad (\text{A.10})$$

where $\Delta \equiv \Delta\rho/\rho_a$ and the tilde ('~') denotes non-dimensional variables. The initial conditions become

$$\tilde{r} = 1, \tilde{z} = 0, \text{ and } \tilde{w} = \frac{w_0}{(r_0g'_0)^{1/2}} \text{ at } \tilde{t} = 0. \quad (\text{A.11})$$

Noting that $|\tilde{w}| = d\tilde{z}/d\tilde{t}$ and using Eq. (A.10), (A.8) reduces to

$$\frac{d\tilde{r}}{d\tilde{z}} = \alpha, \quad (\text{A.12})$$

which shows that the linear growth of a turbulent thermal is a direct consequence of the entrainment assumption, and remains valid for non-Boussinesq thermals.

Using the conservation of buoyancy (Eq. A.10), integration of the momentum Eq. (A.9) gives

$$(\tilde{r}^3 + \Delta)\tilde{w} = Fr^{1/2} + \tilde{r}, \quad (\text{A.13})$$

where

$$Fr = \frac{(1 + \Delta)^2 w_0^2}{\Delta g r_0} = \left(\frac{\ell_M}{r_0}\right)^4. \quad (\text{A.14})$$

The Morton length, ℓ_M , which in this case is

$$\ell_M = \left(\frac{4\pi}{3}\right)^{-1/4} \frac{(M_0/\rho_a)^{1/2}}{B_0^{1/4}} = \left[\frac{(1 + \Delta)^2 w_0^2 r_0^3}{g_0}\right]^{1/4}, \quad (\text{A.15})$$

represents the distance in which the initial momentum dominates over buoyancy-induced momentum. Again noting that $\tilde{w} = d\tilde{z}/d\tilde{t}$ and using $\tilde{r} = 1 + \alpha\tilde{z}$, Eq. (A.13) can be rewritten as

$$\frac{d}{d\tilde{t}} \left(\Delta\tilde{z} + \frac{1}{4\alpha} (1 + \alpha\tilde{z})^4 \right) = Fr^{1/2} + \tilde{t}, \quad (\text{A.16})$$

which integrates once to yield

$$\Delta\tilde{z} + \frac{1}{4\alpha} \left[(1 + \alpha\tilde{z})^4 - 1 \right] = \left(Fr^{1/2} \tilde{t} + \frac{1}{2} \tilde{t}^2 \right) \quad (\text{A.17})$$

$$= \frac{1}{2} \left[\left(\tilde{t} + Fr^{1/2} \right)^2 - Fr \right]. \quad (\text{A.18})$$

An exact analytical expression for the velocity as a function of \tilde{z} can be obtained by combining Eqs. (A.13) and Eq. (A.18):

$$\tilde{w} = \frac{1}{\Delta + (1 + \alpha\tilde{z})^3} \left\{ Fr + 2\Delta\tilde{z} + \frac{1}{2\alpha} \left[(1 + \alpha\tilde{z})^4 - 1 \right] \right\}^{1/2}. \quad (\text{A.19})$$

In dimensional form, Eq. (A.19) is

$$w = \frac{\sqrt{g_0 r_0}}{\Delta + \left(1 + \alpha \frac{z}{r_0}\right)^3} \left\{ Fr + 2\Delta \frac{z}{r_0} + \frac{1}{2\alpha} \left[\left(1 + \alpha \frac{z}{r_0}\right)^4 - 1 \right] \right\}^{1/2}. \quad (\text{A.20})$$

The first term inside the curly brackets in Eq. (A.20) is due to the initial momentum, and is equal to zero if $w_0 = 0$. The second term comes from the finite initial density contrast between the turbulent thermal and the ambient fluid, and vanishes for Boussinesq thermals. The last term in the brackets is the contribution of the buoyancy, and is often the only term considered in the literature.

Eq. (A.19) has limits for small z and large z , which we give here in dimensional form.

For small z , there is two possible limiting solutions depending on whether z is large or small compared to $r_0 Fr/[2(1 + \Delta)]$. For $z \ll \min\left(\frac{r_0}{\alpha}, \frac{\Delta+1}{3\alpha} r_0, \frac{Fr}{2(1+\Delta)} r_0\right)$,

$$w \approx w_0 + w_0 \left(\frac{1 + \Delta}{Fr} - \frac{3\alpha}{1 + \Delta} \right) \frac{z}{r_0} \quad (\text{A.21})$$

In Eq. (A.21), the second term on the RHS is the difference between the acceleration due to buoyancy, and a decrease of specific momentum due to the entrainment of ambient fluid (dilution of initial momentum). The initial evolution of the thermal corresponds to a phase of either acceleration or deceleration, depending on whether Fr is smaller or larger than $(\Delta + 1)^2/3\alpha$, or equivalently, whether w_0 is smaller or larger than $\sqrt{(g_0 r_0)/(3\alpha)}$.

If $z \ll \min\left(\frac{r_0}{\alpha}, \frac{\Delta+1}{3\alpha} r_0\right)$, but $z \gg \frac{Fr}{2(1+\Delta)} r_0$, then

$$w \approx \left(\frac{2g_0}{\Delta + 1} \right)^{1/2} z^{1/2}. \quad (\text{A.22})$$

Here the initial momentum is negligible and this corresponds simply to a buoyancy-induced acceleration phase.

Finally, for large z , i.e. for $z \gg \max\left(\frac{r_0}{\alpha}, \Delta^{1/3} \frac{r_0}{\alpha}, \frac{2^{1/4}}{\alpha^{3/4}} \ell_M\right)$,

$$w \approx \left(\frac{\Delta g r_0^3}{2\alpha^3} \right)^{1/2} \frac{1}{z}. \quad (\text{A.23})$$

This limiting solution for large z is independent of the initial conditions, and corresponds to the self-similar solution predicted by dimensional analysis. The thermal is expected to reach self-similar behavior when the effect of initial momentum becomes negligible (i.e. for $z \gg 2^{1/4} \alpha^{-3/4} \ell_M$), and when the effect of the finite initial size becomes negligible (i.e. for $z \gg r_0/\alpha$). This later condition is equivalent to the requirement that the volume $V(z)$ be large compared to the initial volume.

References

- Baker, J., Bizzarro, M., Wittig, N., Connelly, J., Haack, H., 2005. Early planetesimal melting from an age of 4.5662 gyr for differentiated meteorites. *Nature* 436, 1127–1131.
- Batchelor, G., 1954. Heat convection and buoyancy effects in fluids. *Q. J. R. Meteorolog. Soc.* 80, 339–358.
- Bjorkman, M., Holsapple, K., 1987. Velocity scaling impact melt volume. *Int. J. Impact Eng.* 5, 155–163.
- Bottke, W.F., Nesvorný, D., Grimm, R.E., Morbidelli, A., O'Brien, D.P., 2006. Iron meteorites as remnants of planetesimals formed in the terrestrial planet region. *Nature* 439, 821–824.
- Boyet, M., Carlson, R.W., 2005. ^{142}Nd evidence for early (>4.53 ga) global differentiation of the silicate Earth. *Science* 309, 576–581.
- Boyet, M., Blichert-Toft, J., Rosig, M., Storey, M., Télouk, P., Albarède, F., 2003. ^{142}Nd evidence for early earth differentiation. *Earth Planet. Sci. Lett.* 214, 427–442.
- Buehler, J., Papantonou, D., 2001. On the motion of suspension thermals and particle swarms. *J. Hydraul. Res.* 643–653.
- Bush, J.W.M., Thurber, B.A., Blanchette, F., 2003. Particle clouds in homogeneous and stratified environments. *J. Fluid Mech.* 489, 29–54.
- Caro, G., Bourdon, B., Birck, J.L., Moorbath, S., 2003. ^{146}Sm – ^{142}Nd evidence from Isua metamorphosed sediments for early differentiation of the Earth's mantle. *Nature* 423, 428–432.
- Caro, G., Bourdon, B., Wood, B.J., Corgne, A., 2005. Trace-element fractionation in Hadean mantle generated by melt segregation from a magma ocean. *Nature* 436, 246–249.
- Chabot, N., Draper, D., Agee, C., 2005. Conditions of core formation in the Earth: constraints from Nickel and Cobalt partitioning. *Geochim. Cosmochim. Acta* 69, 2141–2151.
- Chandrasekhar, S., 1961. Hydrodynamic and hydromagnetic stability. *International Series of Monographs on Physics*. Clarendon, Oxford.
- Chen, H., Middleman, S., 1967. Drop size distribution in agitated liquid–liquid systems. *AIChE J.* 13, 989–995.
- Clift, R., Grace, J.R., Weber, M.E., 1978. Bubbles, Drops and Particles. Academic Press, New York.
- Dahl, T., Stevenson, D., 2010. Turbulent mixing of metal and silicate during planet accretion—and interpretation of the Hf–W chronometer. *Earth Planet. Sci. Lett.* 295, 177–186.
- de Wijs, G.A., Kresse, G., Vocadlo, L., Dobson, D., Alfe, D., Gillan, M.J., Price, G.D., 1998. The viscosity of liquid iron at the physical conditions of the Earth's core. *Nature* 392, 805–807.
- Dietrich, W.E., 1982. Settling velocity of natural particles. *Water Resour. Res.* 18, 1615–1626.
- Diez, F., Sangras, R., Faeth, G., Kwon, O., 2003. Self-preserving properties of unsteady round buoyant turbulent plumes and thermals in still fluids. *J. Heat Transfer* 125, 821–830.
- Escudier, M., Maxworthy, T., 1973. On the motion of turbulent thermals. *J. Fluid Mech.* 61, 541–552.
- Halliday, A., 2004. Mixing, volatile loss and compositional change during impact-driven accretion of the earth. *Nature* 427, 505–509.
- Halliday, A., 2008. A young moon-forming giant impact at 70–110 million years accompanied by late-stage mixing, core formation and degassing of the earth. *Philos. Trans. R. Soc. A* 366, 4163–4181.
- Hinze, J., 1955. Fundamentals of the hydrodynamic mechanism of splitting in dispersion processes. *AIChE J.* 1, 289–295.
- Ichikawa, H., Labrosse, S., Kurita, K., 2010. Direct numerical simulation of an iron rain in the magma ocean. *J. Geophys. Res.* 115, B01404.
- Karato, S., Murthy, V.R., 1997. Core formation and chemical equilibrium in the earth—I. Physical considerations. *Phys. Earth Planet. Inter.* 100, 61–79.
- Karki, B., Stixrude, L., 2010. Viscosity of MgSiO_3 liquid at earth's mantle conditions: implications for an early magma ocean. *Science* 328, 740–742.
- Kleine, T., Münker, C., Mezger, K., Palme, H., 2002. Rapid accretion and early core formation on asteroids and the terrestrial planets from Hf–W chronometry. *Nature* 418, 952–955.
- Kleine, T., Mezger, K., Palme, H., Münker, C., 2004. The W isotope evolution of the bulk silicate earth: constraints on the timing and mechanisms of core formation and accretion. *Earth Planet. Sci. Lett.* 228, 109–123.
- Kokubo, E., Ida, S., 1998. Oligarchic growth of protoplanets. *Icarus* 131, 171–178.

- Li, J., Agee, C., 1996. Geochemistry of mantle–core differentiation at high pressure. *Nature* 381, 686–689.
- Liebske, C., Schmickler, B., Terasaki, H., Poe, B.T., Suzuki, A., Funakoshi, K., Ando, R., Rubie, D.C., 2005. Viscosity of peridotite liquid up to 13 GPa: implications for magma ocean viscosities [rapid communication]. *Earth Planet. Sci. Lett.* 240, 589–604.
- Melosh, H.J., 1990. Giant Impacts and the Thermal State of the Early Earth. , pp. 69–83.
- Monteux, J., Ricard, Y., Coltice, N., Dubuffet, F., Ulvrova, M., 2009. A model of metal–silicate separation on growing planets. *Earth Planet. Sci. Lett.* 287, 353–362.
- Morton, B.R., Taylor, G., Turner, J.S., 1956. Turbulent gravitational convection from maintained and instantaneous sources. *Proceedings of the Royal Society of London: Mathematical and Physical Sciences, Ser. A*, 234, pp. 1–23.
- Murthy, V.R., 1991. Early differentiation of the earth and the problem of mantle siderophile elements: a new approach. *Science* 253, 303–306.
- Nimmo, F., Agnor, C., 2006. Isotopic outcomes of N-body accretion simulations: constraints on equilibration processes during large impacts from Hf/W observations. *Earth Planet. Sci. Lett.* 243, 26–43.
- Nimmo, F., O'Brien, D., Kleine, T., 2010. Tungsten isotopic evolution during late-stage accretion: constraints on earth–moon equilibration. *Earth Planet. Sci. Lett.* 243, 26–43.
- Noh, Y., Fernando, H., 1993. The transition in the sedimentation pattern of a particle cloud. *Phys. Fluids A* 5, 3049–3055.
- Olson, P., Weeraratne, D., 2008. Experiments on metal–silicate plumes and core formation. *Philos. Trans. R. Soc. A* 366, 4253–4271.
- Pierazzo, E., Melosh, H.J., 2000. Melt production in oblique impacts. *Icarus* 145, 252–261.
- Pierazzo, E., Vickery, A.M., Melosh, H.J., 1997. A reevaluation of impact melt production. *Icarus* 127, 408–423.
- Reese, C.C., Solomatov, V.S., 2006. Fluid dynamics of local martian magma oceans. *Icarus* 184, 102–120.
- Ricard, Y., Šrámek, O., Dubuffet, F., 2009. A multi-phase model of runaway core–mantle segregation in planetary embryos. *Earth Planet. Sci. Lett.* 284, 144–150.
- Richards, J., 1965. Puff motions in unstratified surroundings. *J. Fluid Mech.* 21, 97–106.
- Ringwood, A., 1966. Chemical evolution of the terrestrial planets. *Geochim. Cosmochim. Acta* 30, 41–104.
- Rubie, D., Melosh, H., Reid, J., Liebske, C., Richter, K., 2003. Mechanisms of metal–silicate equilibration in the terrestrial magma ocean. *Earth Planet. Sci. Lett.* 205, 239–255.
- Rudge, J., Kleine, T., Bourdon, B., 2010. Broad bounds on earth's accretion and core formation constrained by geochemical models. *Nat. Geosci.* 3, 439–443.
- Samuel, H., Tackley, P.J., Evonuk, M., 2010. Heat partitioning in terrestrial planets during core formation by negative diapirism. *Earth Planet. Sci. Lett.* 290, 13–19.
- Spera, F., Ghiorso, M., Nevins, D., 2010. Structure, thermodynamic and transport properties of liquid MgSiO₃: comparison of molecular models and laboratory results. *Geochim. Cosmochim. Acta* 75, 1272–1296.
- Šrámek, O., Ricard, Y., Dubuffet, F., 2010. A multiphase model of core formation. *Geophys. J. Int.* 181, 198–220.
- Stevenson, D.J., 1990. Fluid dynamics of core formation. *Origin of the Earth*. Oxford University Press, pp. 231–249.
- Tennekes, H., Lumley, J.L., 1972. *First Course in Turbulence*.
- Terada, A., Ida, Y., 2007. Kinematic features of isolated volcanic clouds revealed by video records. *Geophys. Res. Lett.* 34, L01305.
- Tonks, W.B., Melosh, H.J., 1993. Magma ocean formation due to giant impacts. *J. Geophys. Res.* 98, 5319–5333.
- Turner, J., 1969. Buoyant plumes and thermals. *Annu. Rev. Fluid Mech.* 1, 29–44.
- Turner, J.S., 1980. *Buoyancy Effects in Fluids*. Cambridge University Press.
- Villiermaux, E., 2007. Fragmentation. *Annu. Rev. Fluid Mech.* 39, 419–446.
- Wood, B., Walter, M., Wade, J., 2006. Accretion of the earth and segregation of its core. *Nature* 441, 825–833.
- Yamamoto, H., Watson, M., Phillips, J.C., Bluth, G.J., 2008. Rise dynamics and relative ash distribution in vulcanian eruption plumes at Santiaguito volcano, Guatemala, revealed using an ultraviolet imaging camera. *Geophys. Res. Lett.* 35, L08314.
- Yin, Q., Jacobsen, S., Yamashita, K., Blichert-Toft, J., Telouk, P., Albarede, F., 2002. A short timescale for terrestrial planet formation from Hf/W chronometry of meteorites. *Nature* 418, 949–952.
- Yoshino, T., Walter, M.J., Katsura, T., 2003. Core formation in planetesimals triggered by permeable flow. *Nature* 422, 154–157.